Comparison between measured and calculated bistatic RCS data on a rough metallic background surface

JONAS RAHM, MAGNUS GUSTAFSSON, MAGNUS HERBERTHSON,
STEFAN NILSSON, ANDERS ÖRBOM AND ERIK ZDANSKY

FOI, Swedish Defence Research Agency, is a mainly assignment-funded agency under the Ministry of Defence. The core activities are research, method and technology development, as well as studies conducted in the interests of Swedish defence and the safety and security of society. The organisation employs approximately 1000 personnel of whom about 800 are scientists. This makes FOI Sweden's largest research institute. FOI gives its customers access to leading-edge expertise in a large number of fields such as security policy studies, defence and security related analyses, the assessment of various types of threat, systems for control and management of crises, protection against and management of hazardous substances, IT security and the potential offered by new sensors.

FOI
Defence Research Agency
Information Systems
P.O. Box 1165
SE-581 11 Linköping

Phone: +46 13 37 80 00
Fax: +46 13 37 81 00

www.foi.se

FOI-R--3102--SE Technical report
ISSN 1650-1942 Oktober 2010

Information Systems

Jonas Rahm, Magnus Gustafsson, Magnus Herberthson, Stefan Nilsson, Anders Örbom and Erik Zdansky

Comparison between measured and calculated bistatic RCS data on a rough metallic background surface

Titel	Jämförelser mellan uppmätta och beräknade bistatiska RCS data för en skrovlig metallisk bakgrundsyta
Title	Comparison between measured and calculated bistatic RCS data on a rough metallic background surface
Rapportnr/Report no	FOI-R--3102--SE
Rapporttyp Report Type	Teknisk rapport Technical report
Sidor/Pages	32 p
Månad/Month	Oktober
Utgivningsår/Year	2010
ISSN	ISSN 1650-1942
Kund/Customer	FM
Kompetenskloss	Sensor- och signaturteknik
Projektnr/Project no	E3094
Godkänd av/Approved by	Lars Bohman

FOI, Totalförsvarets Forskningsinstitut
Avdelningen för Informationssystem
Box 1165
581 11 Linköping

FOI, Swedish Defence Research Agency
Information Systems
P.O. Box 1165
SE-581 11 Linköping

Summary

Bistatic radar measurements have been performed on a manufactured rough aluminum surface. The extracted normalized cross sections from the measurements are used to validate two different calculation methods, i.e. the iterative physical optics (IPO) and the integral equation method (IEM).

The IPO method is based on solving the magnetic field integral equation (MFIE) in an iterative procedure and requires a faceted representation of the object. Each iteration step can be considered as an internal interaction contribution to the cross section. The IPO-method is suitable for using on objects that are too large for “exact” methods, e.g. the method of moment (MoM) and the finite difference in time domain (FDTD), and where high frequency methods, e.g. physical optics (PO), do not provide results good enough.

The IEM method is based on solving the Stratton-Chu integral equation by describing the roughness of a surface by two statistical measures, i.e. the correlation length and the height deviation. The output result is given by an average value of the diffuse part of the normalized cross section. The huge advantage with IEM compared to other calculation methods is that IEM is of the order of several magnitudes faster, in terms of CPU-time.

The results from the measurements and IPO are generally in good agreement over all geometries and polarization combinations. The IEM results exhibit very good agreement with IPO and measurement results for some geometries while for other geometries the IEM results will tend to underestimate the normalised cross sections.

The conclusion is that the IEM method has potential to be used to model backgrounds and target-background interaction contributions. Further investigations have to be made concerning variance measures of the diffuse part of the normalized cross section, how to include material properties into IEM and how to combine other methods, e.g. PO, with IEM to be able to make calculations on large scenarios.

Keywords: radar, bistatic, reflectivity, RCS, radar calibration, Gauss surface, X-band, Lilla Gåra

Sammanfattning

Bistatiska radar mätningar har utförts på en tillverkad och skrovlig aluminiumyta. Den normaliserade målytan från mätningarna använd för att validera två olika beräkningsmetoder, dvs iterativ fysikalisk optik (IPO) och integralekvationsmetoden (IEM).

IPO metoden baseras på att lösa den magnetiska fält integral ekvationen (MFIE) på ett iterativt sätt och förutsätter en facetterad beskrivning av objektet. Varje iterationssteg kan betraktas som ett internt reflektionsbidrag till den totala normerade målarean. IPO-metoden lämpar sig att användas på objekt som är för stora för mer ”exakta” metoder, som t ex momentmetoden och finita differens metoden i tidsdomän, och där högfrekvensmetoder, t ex fysikalisk optik, inte ger resultat med tillräckligt god noggrannhet.

IEM metoden baseras på att lösa Stratton-Chu integral ekvationen genom att beskriva den skrovliga ytan med två statistiska parametrar, dvs korrelationslängd och höjdstandardavvikelse. Resultatet från IEM ges av ett medelvärde av den diffusa delen av den normerade målarean. Den stora fördelen med IEM jämfört med andra beräkningsmetoder är framförallt att metoden är mycket snabb.

Jämförelserna mellan mät- och IPO-resultaten visar på mycket god överensstämmelse för alla uppmätta mätgeometrier och polarisations kombinationer. IEM resultaten uppvisar mycket god överensstämmelse med mätdata för några mätgeometrier medans för andra geometrier uppvisar IEM resultaten en underskattning av den normerade målarean.

Slutsatsen är att IEM metoden har en god potential för att kunna användas för beräkning av dels bakgrundsklotter och dels som en del då mål-bakgrundsbidraget av målarean beräknas. Ytterligare undersökningar behöver utföras av IEM för att studera hur stort spridningsmåttet (variansen) är från det erhållna medelvärdet på målarean, hur man inför materialegenskaper i metoden samt hur man kombinerar IEM med andra metoder, t ex fysikalisk optik, för att kunna utföra beräkningar på större scenarier.

Nyckelord: radar, bistatisk, reflektivitet, RCS, radarmålarea, radarkalibrering, Gaussyta, X-band, Lilla Gåra

Content

1 Introduction 6

2 Measurement 7

2.1 Brief presentation of the measurements 7

3 Calculations 14

3.1 Integral Equation Method (IEM) 14

3.1.1 IEM Theory 14
3.1.2 Near field compensation of the IEM 16

3.2 Iterative Physical Optics (IPO) 19

3.2.1 IPO Theory 19
3.2.2 Mesh settings for the reference surface 22

4 Results 23

5 Analysis 27

6 Summary and conclusions 28

7 References 29

Appendix A: Measured reflectivity 31

1 Introduction

Signature data are used in many civil and military applications, e.g. for optimization of sensor performance, development of automatic target recognition (ATR) algorithms, optimization of protection systems mounted on different vehicles and stealth design, to mention just a few. Signature data can be measured or/and calculated. Measurements have the advantage to give reliable and accurate data. The disadvantages are that measurements are relatively expensive and time consuming activities and it is relatively common that the measurement only will cover a small portion of the angular and frequency region of interest. Furthermore, it can be difficult to cover different scenes, e.g. a vehicle in different backgrounds. A complementary method is to calculate the signature. The advantages are that one easily can cover all frequency and angular regions and, in addition, put the object in different backgrounds. However, to be able to perform such calculations one has to introduce approximations in the models which may affect the results. The challenge is to find models and methods that give sufficiently accurate signature results for different applications and at the same time not overload the memory limitations and/or makes the computational time unreasonable long.

For these reasons, Sweden (FOI) and France (ONERA and DGA Celar) jointly decided to address a work programme concerning “New models for radar targets and environment” in 2008. The objectives are:

- To get a better theoretical understanding of complicated scattering phenomena such as target-background interaction.
- To develop a method which models bistatic scattering which can be used in simulation software packages.
- To create a set of reference measurements covering essential aspects of the theory.

The distribution of tasks between the Swedish and the French part is described in reference [1]. The general agreement is that FOI will contribute with bistatic measurements on different backgrounds and DGA Celar will contribute with monostatic measurements on targets over different backgrounds. The measurements are done to validate new background models.

This report presents comparisons between calculated and measured bistatic data of a rough metallic reference background sample. The measurements of the reference surface were performed in 2008 and 2009. The measurement procedure, equipment and result are given in references [3-4].

The bistatic calculation methods that have been used are the Integral Equation Model (IEM) and the Iterative Physical Optics (IPO).

The Swedish participation in this work is part of an assignment from the Swedish armed forces to do research within the field of signature modelling.

2 Measurement

The measurement equipment, procedure, analysis and results are presented in detail in references [3-4]. Therefore there will be just a brief presentation of it in this report.

2.1 Brief presentation of the measurements

The RCS measurements were conducted at Lilla Gåra [4-5]. Lilla Gåra is the FOI's outdoor test range for coherent broadband RCS and antenna measurements. The measurements were performed at the bistatic arc, see Figure 1. The arc consists of a frame structure that supports the arc. The arc consist of two parts, one half arc and one quarter arc that can be rotated around zenith of the half arc, see Figures 1 and 2. The arc has an inner radius of 3.3 meters and can carry antenna wagons that can be moved independently of each other. The bistatic arc is placed over the centre of a turntable used to rotate the sample while collecting data. Figures 2 and 3 show the angle definitions used in the report.

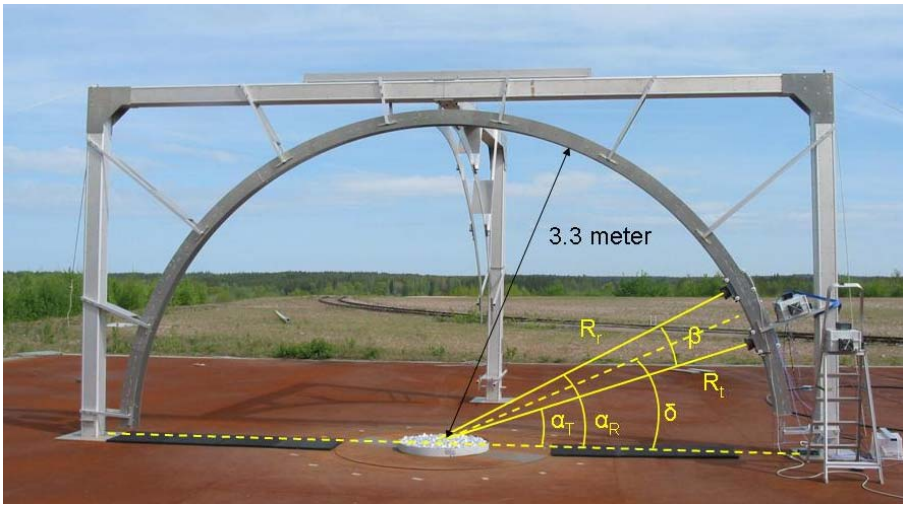

Figure 1. The bistatic arc has an inner radius of 3.3 m and can carry antenna wagons that can be moved independent of each other. Also marked are nominal angles in the plane of incidence, the transmitter and receiver depression angles, α_T and α_R, the bistatic angle, β, and the bisector depression angle δ.

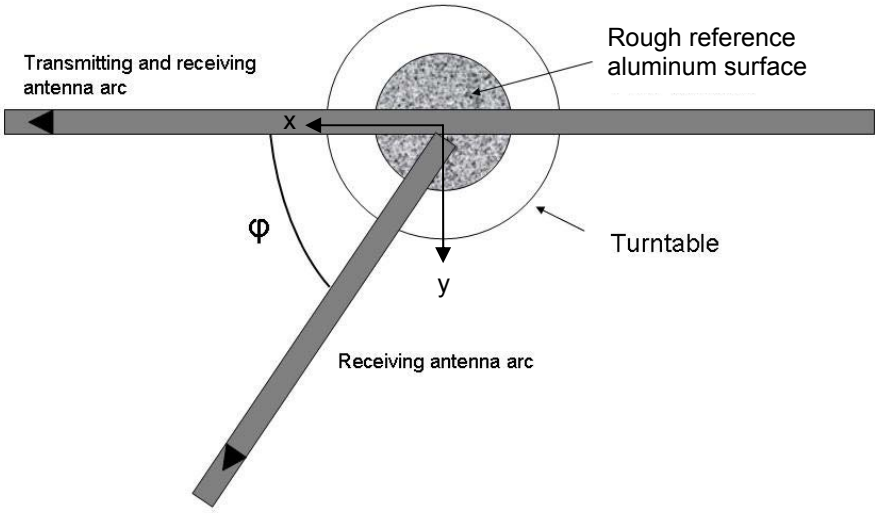

Figure 2. A schematic overview of the whole arc structure. Also marked is the angle φ which represents the angle between the quarter arc and the full arc.

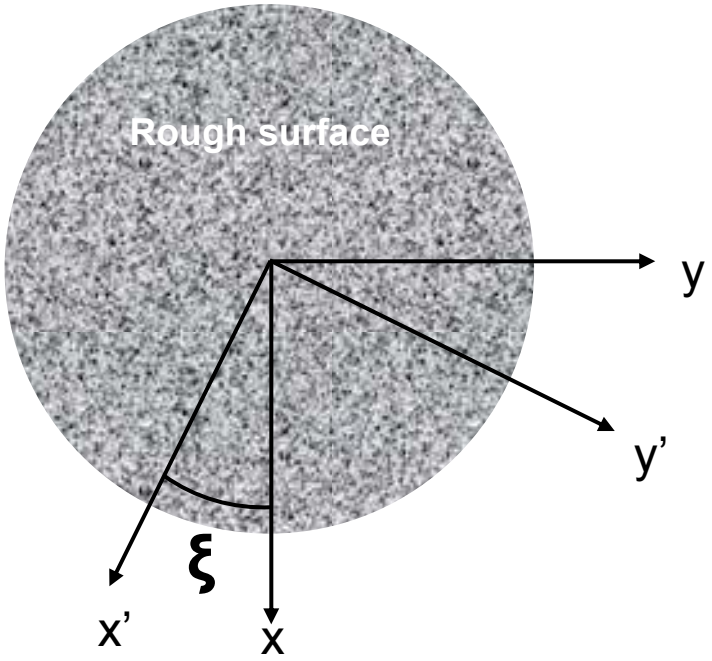

Figure 3. An overview of the rough surface with the rotation angle definition. The x'y' coordinate system is object fixed while the xy-system is fixed relative to the arc. Thus, the angle ξ represents the angle which the rough surface is rotating.

Figure 4 (left) shows the antennas mounted on the antenna wagons and placed in the arc. The boxes behind the antennas (transmitter and receiver) contain optical links and amplifiers. The temperature in the boxes is stabilized to prevent thermal drifts in the optical links and amplifiers. The right picture in Figure 4 (right) shows a view from the antennas. The black squares are radar absorbing material plates which are put there to reduce multiple scattering contributions to the total RCS.

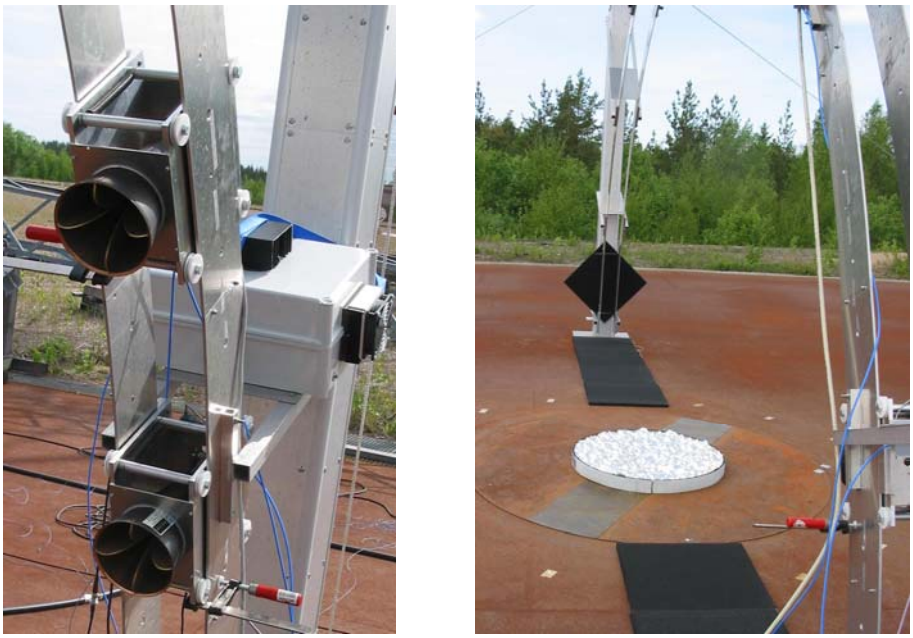

Figure 4. The left picture shows the antennas mounted on the arc. The box behind the antennas is the transmitting climate box containing an optical link and an amplifier. Right picture shows a view from the antenna. The black plates are absorbents (RAM) used to reduce background contributions.

The metallic rough surface used for these measurements is made of solid aluminium and has a diameter of 0.9 meter, see Figure 5. The surface profile was generated according to the spectrum method used in [6]. The roughness of the surface follows a Gaussian distribution function with a correlation length, L, of 0.0191 meters and a height variance, σ_H, of 0.0072meters. This corresponds to kL= 4 and $k\sigma_H$=1.5 at 10 GHz where k is the wave number. The surface was manufactured from an aluminium block by using a numerically controlled milling machine.

Figure 5. The rough aluminium surface. The diameter is 0.9 meter.

The parameters presented below have been used for all measurements.

Frequencies:	8-12 GHz in 4 MHz steps, i.e. 1001frequency steps.
Polarisation:	HH and VH (i.e. the first and second letter correspond to the transmitted and the received polarization direction respectively), see Figure 7 for the direction definition.
Measurement range:	$\mathbf{R}_{transmitter} = \mathbf{R}_{receiver} = 3.21$ meters measured from the antenna fronts to the centre of the turntable.
Antenna positions:	See table in appendix A and angle definitions in Figure 2 and 3.
Object rotation angles (ξ):	For each antenna position combination the turntable (background sample) will rotate ξ = 0-359.95˚ in 0.05˚ step, i.e. 7200 positions.

The definition of the polarisation directions (i.e. the direction of transmitted and received E-field vector) are shown in Figure 6.

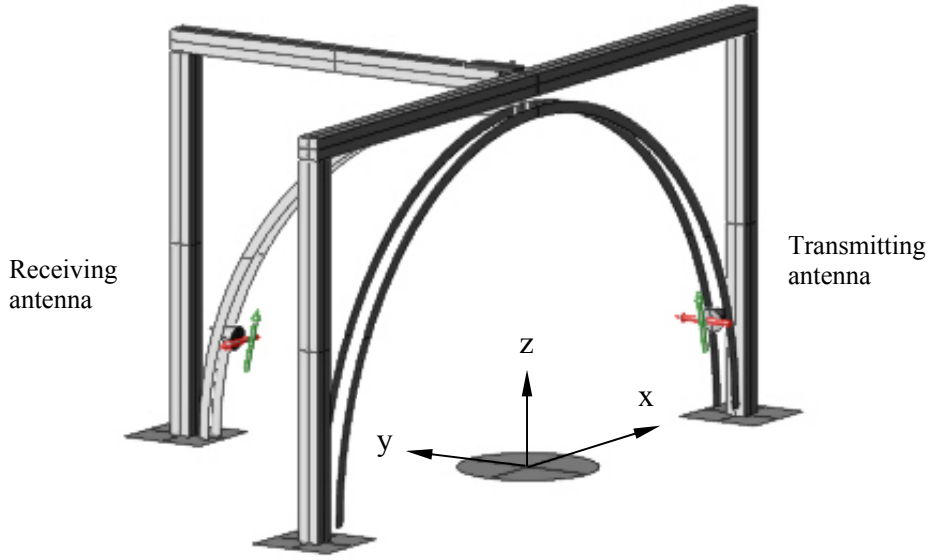

Figure 6. The red arrows define horizontal polarisation (E-field direction) while the green arrows define vertical polarisation.

The polarisation base vectors are, from Figure 6 and according to the angles defined in Figures 1 and 2, defined as

H-pol => $\mathbf{E}_{t,r} = [-\sin\varphi_{t,r} ; \cos\varphi_{t,r} ; 0]$

V-pol => $\mathbf{E}_{t,r} = [-\cos\varphi_{t,r} \cos(90°-\alpha_{t,r}) ; -\sin\varphi_{t,r} \cos(90°- \alpha_{t,r}) ; \sin(90°- \alpha_{t,r})]$

where the indices t and r corresponds to transmitter and receiver, respectively. With this formulation the polarisation is unambiguously defined even for antennas pointing in the nadir direction.

In this measurement campaign we have used an object-free calibration method which is described in references [7-9]. The calibration setup is shown in Figure 7. Two calibration measurements with different polarisation alignments were performed before and after the bistatic measurements. A polarisation switch was mounted on the transmitting antenna enabling us to change the polarisation quickly from one bistatic measurement to another.

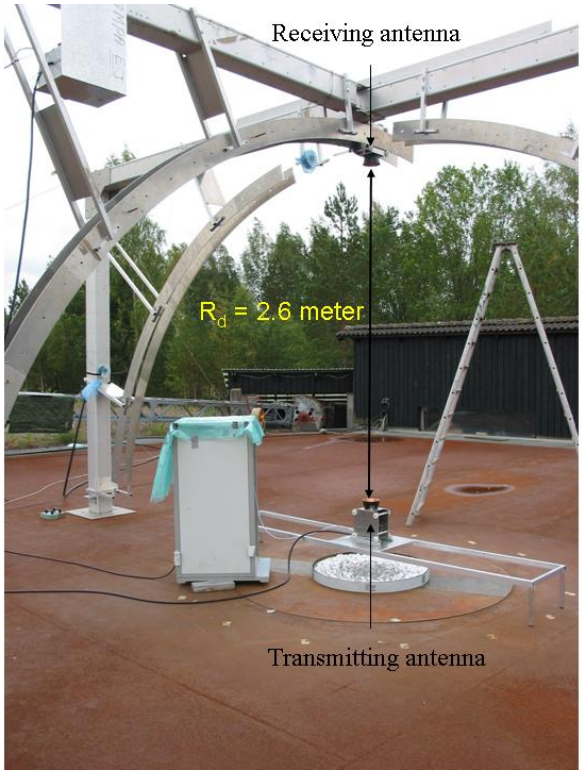

Figure 7. Photo of the calibration geometry. The transmitting antenna is placed on a support standing over the turntable facing the receiving antenna which is placed at the zenith of the arc. The distance between the antenna faces is 2.6 meter.

The measurements were collected while rotating the sample surface 360˚ on the turntable for each bistatic antenna setting. With this procedure it is possible to make two-dimensional bistatic ISAR-images for each bistatic geometry.

Examples of ISAR images are shown in Figures 8a-d. Background contributions do show up in the images but are in general modest in strength and reasonably well separated from the area of interest. Each ISAR image is generated by using an angular region of $\xi \sim \pm 12°$. However, the resolution of the images will decrease with increasing bistatic angle and increasing bisector depression angle, see e.g. Figure 8.

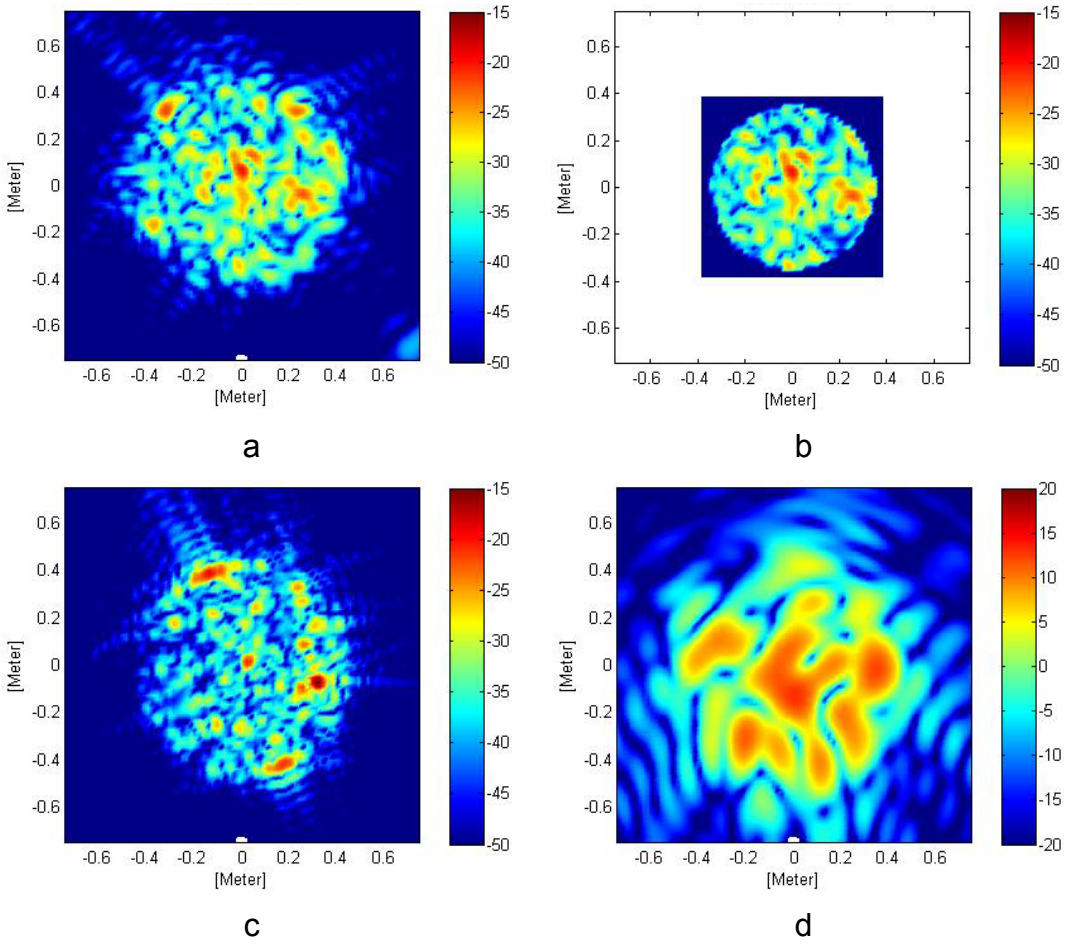

Figures 8a-d. ISAR-images of the Gauss surface measured in different geometries. Top left $\alpha_T = 20^\circ$, $\varphi_T = 0^\circ$, $\alpha_R = 30^\circ$ and $\varphi_R = 90^\circ$. The white dot marks the direction to the bisector position of the radar. Top right the central part of this film frame used for extraction of σ^0. Bottom left, at $\alpha_T = 20^\circ$, $\varphi_T = 0^\circ$, $\alpha_R = 30^\circ$ and $\varphi_R = 45^\circ$. Bottom right, at $\alpha_T = 30^\circ$, $\varphi_T = 0^\circ$, $\alpha_R = 110^\circ$ and $\varphi_R = 0^\circ$, the increase in the bistatic angle and the bisector depression has already reduced the resolution strongly.

In order to remove contributions from fixed scatterers, multipath propagation, edges etc. the ISAR images are cropped so that only the central part of the images remain with pixels outside set to zero. For the aluminum plate the central part was chosen as a circle 0.7 m in diameter.

This procedure can be expected to introduce some truncation artefacts when the images are inverted back to the frequency-angle domain. The artefacts are mainly found at the edges of the frequency range, which are sacrificed.

After the images have been cropped the effective area is calculated. Since distance compensation was included already in the generation of the ISAR images only the directivity of the antennas needs to be taken into account. The transmitting and receiving antennas are identical and the antenna pattern has been measured. From these pattern measurements the radar footprints are calculated and used to make corrections for the effective area. Examples of footprints (transmitter, receiver and the product, i.e. the radar footprint) are shown in Figure 9.

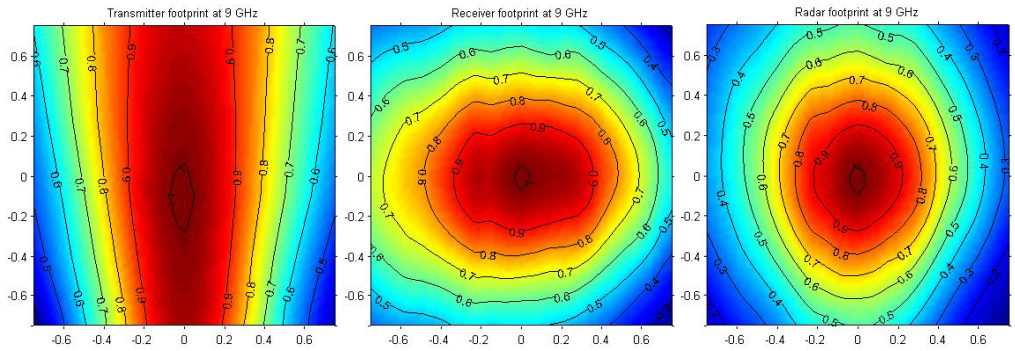

Figure 9. Example of calculated footprints for the transmitter, the receiver and their product for the geometry α_T=10°, φ_T=0°, α_R=50°and φ_R=90° at 9 GHz. Contours mark the relative intensity in linear scale. The footprints are cropped like the ISAR frames and then integrated to give the effective area.

The cropped images are inverted back to the frequency-angle space and normalised using the effective areas. Inverted values have been calculated for 0.04 GHz steps in frequency and 1˚ steps in angle. The result is then incoherently averaged over all angles. Figure 10 show examples of this. The outer parts of the frequency range are, as mentioned, affected by truncation artefacts and therefore discarded. A linear fit (of intensities in dB) is then made for the 8.5 to 11.5 GHz frequency range and the fit value at 10 GHz is used as an estimate of the normalised cross section, σ^0, at that geometry.

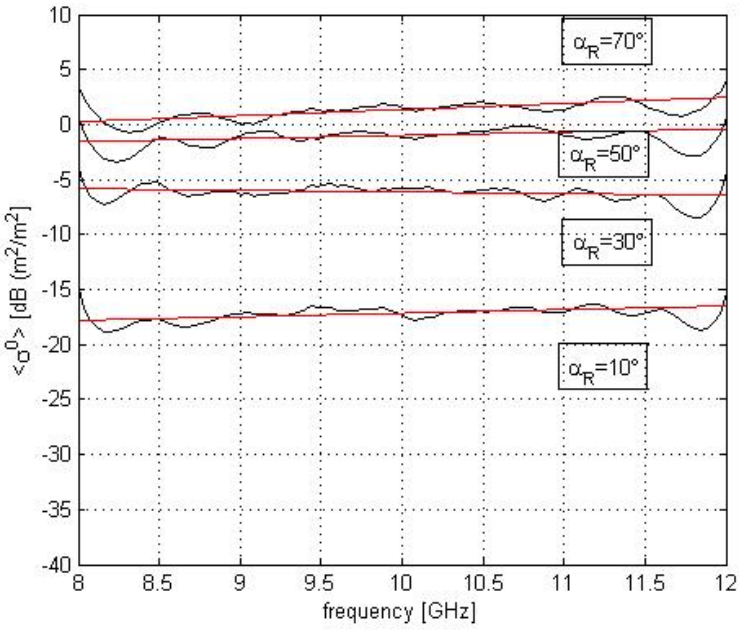

Figures 10. Examples of the reflectivity for four different receiving depression angles as a function of frequency and mean over all turntable directions (film frames). The antenna angles in this case is, α_T = 20˚, φ_T=0˚ and φ_R=90˚and the polarisation is VH. The red line shows the linear fit (of intensities in dB) made for the 8.5 to 11.5 GHz frequency range. The fit value at 10 GHz is used as an estimate of σ^0.

The final results are shown in comparison with calculated results in the result section.

3 Calculations

Bistatic RCS calculations have been performed by using Integral Equation Method (IEM) and Iterative Physical Optics (IPO). The two methods differ relatively much in character. IPO requires a faceted representation of the object while IEM is, in our application, used to calculate the diffuse part of the normalized cross section from a stochastically described rough surface.

3.1 Integral Equation Method (IEM)

The IEM is believed to fulfil the requirements of being a fast and robust method for calculating the average scattered electric field from rough surfaces in a mono- and bistatic receiver transmitter configuration. For this reason, the method is a good candidate to be used to take the target-background interaction contributions into account. The method is based on calculating the induced current on statistically described surfaces in contrast to more CPU-time consuming methods which assume a CAD-representation of a scene. The roughness of the surface is described by different stochastic height distribution functions (e.g. Gaussian) and correlation functions. The height distribution functions are commonly described by the standard height deviation, σ_H and the correlation functions by the correlation length, L. Thus by using the IEM it is possible to calculate the normalised ground scattering coefficient, σ_0, for a surface described by a height distribution and a correlation function. However, there are several variants of IEM in the literature, e.g. with and without shadowing functions and with and without multiple reflections. We are using an IEM variant that includes shadowing and excludes multiple reflections.

3.1.1 IEM Theory

The IEM is described in many references; see e.g. references [10-13]. The method was developed by Fung in the 1990:s and have been extended and developed during the last decade to take e.g. shadowing and multiple scattering effects into account.

In this report we briefly describe the underlying approximation of the IEM. For a more detail description of the method the reader is referred to the references above. Figure 11 shows the scattering problem to solve.

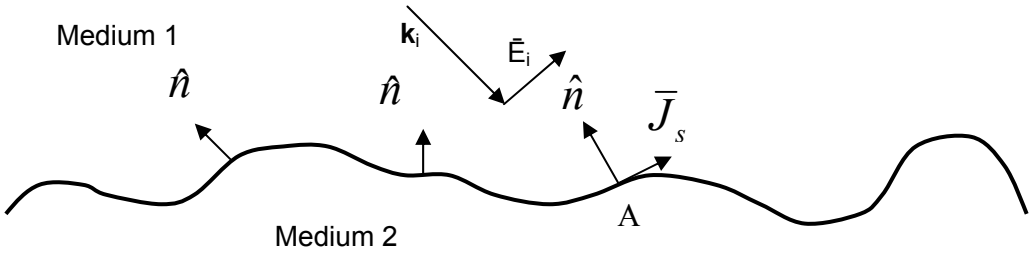

Figure 11. The geometry of the scattering problem to solve, where $\mathbf{k}_i$ *is the incident wave vector,* $\bar{E}_i$ *is the electric field vector of the incident wave,* $\hat{n}$ *are the normal vectors of the surface and* $\bar{J}_s$ *is the induced current vector at the surface. The roughness of the surface of medium 2 is described by two statistical measures, namely the correlation length (L) and the height deviation (*σ_H*).*

The total tangential surface field at point A is given by the Stratton-Chu integral equation.

$$\hat{\mathbf{n}}(\mathbf{r})\times\mathbf{E}(\mathbf{r}) = 2\hat{\mathbf{n}}(\mathbf{r})\times\mathbf{E}^i(\mathbf{r}) - \frac{2}{4\pi}\hat{\mathbf{n}}(\mathbf{r})\times\int_S \mathbf{M}(\mathbf{r}',\mathbf{r})\,\mathrm{d}s', \qquad \mathbf{r}\in S \quad (1)$$

where $\mathbf{M}(\mathbf{r}',\mathbf{r}) = ik\eta(\hat{\mathbf{n}}(\mathbf{r}')\times\mathbf{H}(\mathbf{r}'))G - (\hat{\mathbf{n}}(\mathbf{r}')\times\mathbf{E}(\bar{\mathbf{r}}'))\times\nabla' G - (\hat{\mathbf{n}}(\mathbf{r}')\cdot\mathbf{E}(\bar{\mathbf{r}}'))\nabla' G$ and $\mathbf{E}(\mathbf{r}')$ and $\mathbf{H}(\mathbf{r}')$ are the electric and magnetic fields on the surface. $\mathbf{E}^i$ is the incident field and G is the free space Green's function and is given by

$$G(k,|\mathbf{r}-\mathbf{r}'|) = \frac{e^{ik|\mathbf{r}-\mathbf{r}'|}}{4\pi|\mathbf{r}-\mathbf{r}'|}$$

η and k represent the wave impedance and the wave vector of medium 1 respectively. By adding and subtracting the factor $\hat{\mathbf{n}}\times\mathbf{E}^r$, where $\mathbf{E}^r$ represents the reflected electric field, on the right hand side of (1) we can write:

$$\hat{\mathbf{n}}\times\mathbf{E} = (\hat{\mathbf{n}}\times\mathbf{E})_k + (\hat{\mathbf{n}}\times\mathbf{E})_c \quad (2)$$

where

$$(\hat{\mathbf{n}}\times\mathbf{E})_k = \hat{\mathbf{n}}\times(\mathbf{E}^i + \mathbf{E}^r)$$

is the so called Kirchhoff term while the term

$$(\hat{\mathbf{n}}\times\mathbf{E})_c = \hat{\mathbf{n}}\times(\mathbf{E}^i - \mathbf{E}^r) - \frac{2}{4\pi}\hat{\mathbf{n}}\times\int\mathbf{M}(\mathbf{r},\mathbf{r}')\,\mathrm{d}s' \quad (3)$$

is the so called complementary term. The latter term can be seen as higher order contributions (cf. iterative physical optics).

From the integral equation (1) approximations of $\mathbf{E}$ and $\mathbf{E}^r$ terms are made. The most fundamental approximation is the physical optics (PO) approximation which states that the reflected and transmitted fields can be written in terms of the incident field at each point on the surface, i.e. the tangent plane approximation. Once these approximations have been made the scattered field from the surface is calculated using a far field integral formula

$$\mathbf{E}^s(\mathbf{r}) = \frac{ik^2 e^{ikR}}{4\pi R}\iint_S(\hat{\mathbf{n}}(\mathbf{r}')\times\mathbf{E}(\mathbf{r}') - \eta_0\hat{\mathbf{r}}\times(\hat{\mathbf{n}}(\mathbf{r}')\times\mathbf{H}(\mathbf{r}')))e^{-ik\hat{\mathbf{r}}\cdot\mathbf{r}'}\mathrm{d}s' \quad (4)$$

where $\mathbf{r} = R\hat{\mathbf{r}}$ is the point of observation and $R >> 2d^2 / \lambda$, d is maximum size of S, $\hat{n}$ is the surface normal and λ is the wavelength.

For the magnetic field $\mathbf{H}(\mathbf{r})$, basically the same formulations and approximations are used. Using (2) and (3) along with the approximations into (4) we get the scattered far field from the surface S.

We are interested in the mean diffuse scattered energy, for combination of incident and received polarisations, described by eq (5), from the surface S. The surface S is therefore described using a stochastic variable described by the parameters σ_H and L mentioned earlier.

$$P_{qp} = \frac{1}{2\eta}(\left\langle \left| E^s_{qp}(\mathbf{r}) E^s_{qp}(\mathbf{r}'') \right| \right\rangle - \left| \left\langle E^s_{qp} \right\rangle \right|^2) \qquad (5)$$

where q and p represents the polarisation direction (H or V) for the transmitter and receiver antenna respectively.

In our case each realisation of S is described by $\mathbf{r}' = x'\hat{\mathbf{x}} + y'\hat{\mathbf{y}} + Z(x', y')\hat{\mathbf{z}}$, where each $Z(x', y') \in N(0, \sigma_h)$, and $N(0, \sigma_h)$ is the normal distribution. The first term of eq (5) involves a quadruple integral of the source points $\mathbf{r}', \mathbf{r}'''$. The surfaces S', S''' are correlated in a known manner, giving the correct correlation function and hence the correlation length L. This means that for a given field point $\mathbf{r}$, $\mathbf{E}^s$ will become a stochastic variable. Hence we can calculate its expectation value $<\mathbf{E}^s>$ and also its variance. As mentioned earlier we are interested in certain combinations of transmitted and received polarisations, (the scattering matrix of S). We get four stochastic variables, one for every combination q,p. For each such variable (defined at $\bar{r}$).

From (5) the ground scattering coefficient is defined as

$$\sigma_0 = \frac{4\pi R^2 P_{qp}}{P^i_q A_0} \qquad (6)$$

where P^i_q is the incident power illuminating the area A_0. R is the far field distance from the surface to the receiver. The left hand side of eq (5) represent so called diffuse energy, that is the scattered energy which is proportional to the illuminated area. The first term of the right hand side of eq (5) is the total scattered energy and the second term is the coherent scattered energy which depends on the shape and size of the illuminated area. Usually this term is very small in all but the specular region of the surface.

In the IEM we have also included the shadowing function by Smith [14]. There are other shadowing functions proposed by Sancer, [15] and Fung [11]. However the shadowing function proposed by Smith produces far better agreements to measurements and IPO than the proposed Sancer shadowing function.

3.1.2 Near field compensation of the IEM

In this section we briefly describe the near field compensation of the IEM. A more detailed description will be published elsewhere.

The scattering expression of the original IEM are derived for farfield. However, the measurements are conducted in the near field of the rough surface. In order to take near field effects into account we expand the IEM-method to include a near field compensation.

Due to the fact that the rough reference surface is spatially extended and the measurement range is relatively short, i.e. ~ 3.3 meters, different parts of the surface will have different incident and scattering geometry angles. Figure 12 shows a schematic illustration of this. This variation of scattering angles is affecting the calculated normalized cross section and can be considered as a near field effect. To take this varying scattering geometry into account, the surface has been subdivided into small areas (dA), see Figure 13. The assumption is that within each subarea the incident and scattering geometry angels are constant.

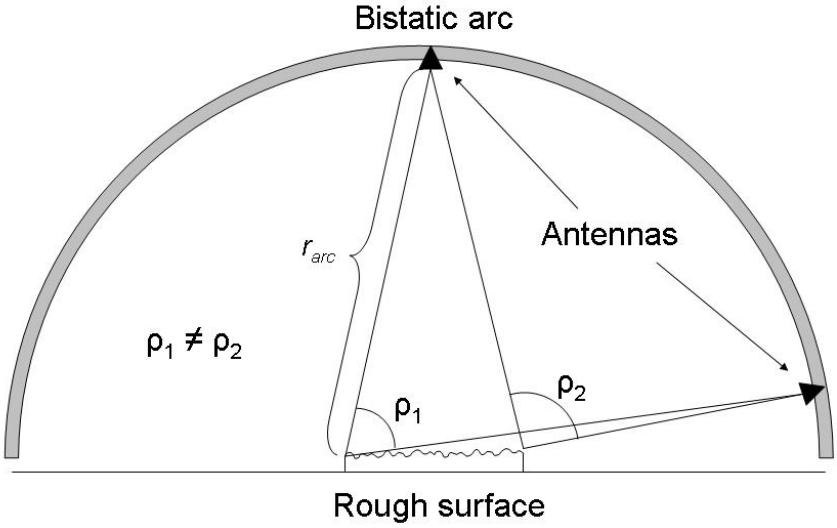

Figure 12. Schematic side view of the measurement setup. The Figure shows that the incident and scattering angels is varying over the rough surface for a fixed antenna setting.

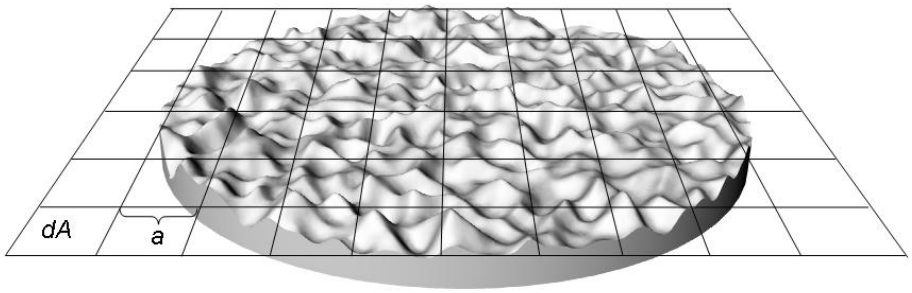

Figure 13. A schematic illustration of how the rough surface is divided into subarea elements that fulfil the far field condition $r_{arc} >> 2a^2/\lambda$.

The area dA is chosen so the far field criteria is fulfilled, i.e. $r_{arc} >> 2a^2/\lambda$, where r_{arc} and a are defined in Figures 12 and 13 and λ is the EM-wavelength.

The total scattered field from the surface, E_{qp}^{s}, can be written as

$$E_{qp}^{s} = \sum_{i=1}^{n} E_{qp}^{s,i} \qquad (7)$$

where n is the number of subareas, dA.

Considering only the diffuse energy of eq (5) the diffuse scattered energy is written as.

$$P_{qp} = \sum_{i=1}^{n} \left\langle \left| E_{qp}^{s,i} \right|^2 \right\rangle \tag{8}$$

Making near field compensation requires that the polarisation is taken into account in an unambiguous way. For that reason we are introducing matrices that transform the polarisation directions from the transmitter to different dA and to the receiver in a proper way. The scattered field, $E^{s,i}$, from the area dA_i can be written as

$$\mathbf{E}^{s,i} = \begin{pmatrix} \hat{\mathbf{e}}_{sh}^{i} & \hat{\mathbf{e}}_{sv}^{i} \end{pmatrix} \begin{pmatrix} \chi_{hh}^{i} & \chi_{hv}^{i} \\ \chi_{vh}^{i} & \chi_{vv}^{i} \end{pmatrix} \begin{pmatrix} \alpha_{hh}^{i} & \alpha_{hv}^{i} \\ \alpha_{vh}^{i} & \alpha_{vv}^{i} \end{pmatrix} \begin{pmatrix} E_{h}^{i} \\ E_{v}^{i} \end{pmatrix} \tag{9}$$

where $E_{h,v}^{i}$ is the incident field in the ON-base $\begin{pmatrix} \hat{\mathbf{e}}_{ih}^{i} & \hat{\mathbf{e}}_{iv}^{i} \end{pmatrix}$ defined by IEM in [10]. $\begin{pmatrix} \hat{\mathbf{e}}_{ih}^{i} & \hat{\mathbf{e}}_{iv}^{i} \end{pmatrix}$ depends on the position from dA_i to the transmitter. $\begin{pmatrix} \hat{\mathbf{e}}_{sh}^{i} & \hat{\mathbf{e}}_{sv}^{i} \end{pmatrix}$ is the ON-base describing the electrical axis of the receiving antenna (relative a given dA_i). The matrix elements α_{qp}^{i} are the scattering coefficients of dA_i. The χ-matrix is the transformation matrix between the ON-bases, given by IEM in [10], describing the scattering from the surface and the $\begin{pmatrix} \hat{\mathbf{e}}_{sh}^{i} & \hat{\mathbf{e}}_{sv}^{i} \end{pmatrix}$-base. The incident field $\begin{pmatrix} E_{h}^{i} \\ E_{v}^{i} \end{pmatrix}$ can be written as

$$\begin{pmatrix} E_{h}^{i} \\ E_{v}^{i} \end{pmatrix} = \begin{pmatrix} \hat{\mathbf{e}}_{ih} & \hat{\mathbf{e}}_{iv} \end{pmatrix} \begin{pmatrix} \beta_{hh}^{i} & \beta_{hv}^{i} \\ \beta_{vh}^{i} & \beta_{vv}^{i} \end{pmatrix} \begin{pmatrix} E_{th}^{i} \\ E_{tv}^{i} \end{pmatrix} \tag{10}$$

where E_{th}^{i}, E_{tv}^{i} are the horizontal and vertical field components in the frame of the transmitting antenna. The β^{i}'s are the projection of the incident field on the $\begin{pmatrix} \hat{\mathbf{e}}_{ih}^{i} & \hat{\mathbf{e}}_{iv}^{i} \end{pmatrix}$ basis.

Using (10) in (9) gives the received field in terms of the transmitted field as

$$\overline{E}^{s,i} = \begin{pmatrix} \hat{\mathbf{e}}_{sh}^{i} & \hat{\mathbf{e}}_{sv}^{i} \end{pmatrix} \begin{pmatrix} \chi_{hh}^{i} & \chi_{hv}^{i} \\ \chi_{vh}^{i} & \chi_{vv}^{i} \end{pmatrix} \begin{pmatrix} \alpha_{hh}^{i} & \alpha_{hv}^{i} \\ \alpha_{vh}^{i} & \alpha_{vv}^{i} \end{pmatrix} \begin{pmatrix} \beta_{hh}^{i} & \beta_{hv}^{i} \\ \beta_{vh}^{i} & \beta_{vv}^{i} \end{pmatrix} \begin{pmatrix} E_{th}^{i} \\ E_{tv}^{i} \end{pmatrix} \tag{11}$$

By choosing the receiving and transmitting polarisation (indicated by p and q) and squaring to get incoherent energy, $\left| E_{qp}^{s,i} \right|^2$, used in (8). We see that $\left| E_{qp}^{s,i} \right|^2$ involves terms like $\alpha_{mn}^{i} \alpha_{pq}^{i*}$ where *m, n, p, q* is either H- or V-polarised. These terms represent the bistatic ground scattering coefficients of the surface.

If *(p,q)* = (*m,n)* these terms are given by IEM as $\sigma_{hh}^{0}, \sigma_{hv}^{0}, \sigma_{vh}^{0}, \sigma_{vv}^{0}$. These are the only terms given by IEM and they do not contain the full information about $\alpha_{mn}^{i} \alpha_{pq}^{i*}$. To include these terms we have enhanced the IEM (to be reported elsewhere).

3.2 Iterative Physical Optics (IPO)

The IPO method is described in the literature, see for example [14-17]. The method requires a mesh representation of the object from which the induced currents can be calculated. Only the area and the normal direction of each facet are used when calculating the induced current for the facets. Having the total current distribution of the object it is possible to calculate the far field amplitude and thus the normalized cross section. Reference [16] shows that the iterative solution procedure may converge when the discretisation resolution of the object is as low as 1/3 of the illuminating wavelength, i.e. at 10 GHz (=> λ = 0.03 meter) the discretisation resolution needs to be ~ 0.01 meter. The benefits of the method are that it is relatively fast and less memory demanding than "exact" methods such as e.g. method of moments, finite element method or/and finite difference time domain method. This makes the IPO-method suitable for using on objects that are too large for "exact" methods and where high frequency methods do not provide results which are good enough. However, even if the method is less memory consuming than the methods described above IPO is still not suitable to use for too large objects or scenes. No near field corrections, similar to those that have been made for the IEM calculations, have been applied. The calculations have been limited to include 3 iterations.

3.2.1 IPO Theory

The common base for IPO is the magnetic field integral equation (MFIE), see equation (12). Considering a perfect electric conducting (PEC) material the surface representation of MFIE can be written as

$$\mathbf{J}_S(\mathbf{r}) = 2\hat{n}(\mathbf{r}) \times \iint \nabla G(k, |\mathbf{r}-\mathbf{r}'|) \times \mathbf{J}_S(\mathbf{r}')dS' + \mathbf{J}_{PO}(\mathbf{r}), \qquad \mathbf{r} \in S \quad (12)$$

where $\mathbf{J}_{PO}(\mathbf{r}) = 2\,\hat{n}(\mathbf{r}) \times \mathbf{H}_i(\mathbf{r})$ is the current density on the surface given by the physical optic approximation and $\mathbf{r}$ and $\mathbf{r}'$ represent the field and source point respectively. The normal direction for the facet is given by $\hat{n}$. Thus, equation (12) describes the current density $\mathbf{J}_S(\mathbf{r})$ on an object for a given incident field $\mathbf{H}_i(\mathbf{r})$. The integral shall be interpreted in the Cauchy principal value sense. The Green's function in free space is given by

$$G(k, |\mathbf{r}-\mathbf{r}'|) = \frac{e^{ik|\mathbf{r}-\mathbf{r}'|}}{4\pi|\mathbf{r}-\mathbf{r}'|} \quad (13)$$

where k is the wave number. A formal solution to the integral equation (12) can be achieved by following the iteration scheme,

$$\begin{cases} \mathbf{J}_S^{n+1}(\mathbf{r}) = 2\hat{n}(\mathbf{r}) \times \iint \nabla G(k, |\mathbf{r}-\mathbf{r}'|) \times \mathbf{J}_S^n(\mathbf{r}')dS' & ,n = 0,1,2... \\ \mathbf{J}_S^0(\mathbf{r}) = \mathbf{J}_{PO}(\mathbf{r}) = 2\hat{n}(\mathbf{r}) \times \mathbf{H}_i(\mathbf{r}) \end{cases} \quad (14)$$

where the total current density on the surface is formally given by

$$\mathbf{J}_S^{Tot}(\mathbf{r}) = \sum_{n=0}^{\infty} \mathbf{J}_S^n(\mathbf{r}) \quad (15)$$

However, the iteration scheme is not guaranteed to converge. Several factors affect the condition of convergence of the iteration scheme (14), e.g. choice of initial currents, discretisation of the object (in terms of meshes per wavelength), type of object and so forth. To improve convergence, (14) will be reformulated. Namely, introduce the partial sums (note the two different kinds of superscript)

$$\mathbf{J}_S^{(n)}(\mathbf{r}) = \sum_{k=0}^{n} \mathbf{J}_S^k(\mathbf{r}), \;\; n = 0,1,2,...$$

so that $\mathbf{J}_S^{(n+1)}(\mathbf{r}) = \mathbf{J}_S^{(n)}(\mathbf{r}) + \mathbf{J}_S^{n+1}(\mathbf{r})$. By summing the n first terms in the iteration (14) above we get

$$\mathbf{J}_S^{(n+1)}(\mathbf{r}) - \mathbf{J}_S^{(0)}(\mathbf{r}) = 2\hat{n}(\mathbf{r}) \times \iint \nabla G(k, |\mathbf{r} - \mathbf{r}'|) \times \mathbf{J}_S^{(n)}(\mathbf{r}') dS', \;\; n = 0,1,2...$$

or

$$\mathbf{J}_S^{n+1}(\mathbf{r}) = -\mathbf{J}_S^{(n)}(\mathbf{r}) + 2\hat{n}(\mathbf{r}) \times \iint \nabla G(k, |\mathbf{r} - \mathbf{r}'|) \times \mathbf{J}_S^{(n)}(\mathbf{r}') dS' + \mathbf{J}_S^{(0)}(\mathbf{r}), \;\; n = 0,1,2... \quad (16)$$

Note that in the recursion (14), each incremental current $\mathbf{J}_S^{n+1}(\mathbf{r})$ depends only on the previous increment $\mathbf{J}_S^{n}(\mathbf{r})$, while in (16), $\mathbf{J}_S^{n+1}(\mathbf{r})$ depends on the whole partial sum $\mathbf{J}_S^{(n)}(\mathbf{r})$. This is a fundamental difference, and it is also what allows us to introduce a relaxation parameter a. Thus for an (arbitrarily) chosen a, $0 < a \leq 1$, (16) is replaced by the iteration

$$\begin{cases} \mathbf{J}_S^{n+1}(\mathbf{r}) = a\left(-\mathbf{J}_S^{(n)}(\mathbf{r}) + 2\hat{n}(\mathbf{r}) \times \iint \nabla G(k, |\mathbf{r} - \mathbf{r}'|) \times \mathbf{J}_S^{(n)}(\mathbf{r}') dS' + \mathbf{J}_S^{(0)}(\mathbf{r})\right), \;\; n = 0,1,2... \\ \mathbf{J}_S^{0}(\mathbf{r}) = \mathbf{J}_{PO}(\mathbf{r}) = 2\hat{n}(\mathbf{r}) \times \mathbf{H}_i(\mathbf{r}) \end{cases} \quad (17)$$

The choice $a = 1$ gives the recursion (14), while $0 < a < 1$ gives an iteration scheme where one takes smaller steps in terms of the updated current. This approach is also used in reference [16], and at least on a heuristic level, this may improve convergence.

It should also be noted that the iteration (17) can be implemented in several different ways. The results presented here are produced under an evaluation of (17) in the simplest possible way. Thus, the surface S considered is divided into N facets, $T_1, \ldots, T_k, \ldots, T_N$ each facet carrying a constant current $\mathbf{J}_S(\mathbf{r}_k)$, $\mathbf{r}_k \in T_k$. Since the current is parallel to the surface, this gives a total number of 2N unknowns. For a particular choice of field point $\mathbf{r}_k \in T_k$, (17) gives the update $\mathbf{J}_S^{n+1}(\mathbf{r}_k) = a\left(-\mathbf{J}_S^{(n)}(\mathbf{r}_k) + 2\hat{n}(\mathbf{r}_k) \times \iint \nabla G(k, |\mathbf{r}_k - \mathbf{r}'|) \times \mathbf{J}_S^{(n)}(\mathbf{r}') dS' + \mathbf{J}_S^{(0)}(\mathbf{r}_k)\right)$. Now, $\mathbf{J}_S^{(n)}(\mathbf{r}'_m)$ is assumed to be constant on each T_m, and by the further assumption that $g(k, |\mathbf{r}_k - \mathbf{r}'|)$ can also be approximated with a constant value when $\mathbf{r}' \in T_m$, the recursion becomes

$$\mathbf{J}_S^{n+1}(\mathbf{r}_k) = a\left(-\mathbf{J}_S^{(n)}(\mathbf{r}_k) + 2\hat{n}(\mathbf{r}_k) \times \left(\nabla G(k, |\mathbf{r}_k - \mathbf{r}'_m|) \times \mathbf{J}_S^{(n)}(\mathbf{r}'_m)\right) | T_m | + \mathbf{J}_S^{(0)}(\mathbf{r}_k)\right) \quad (18)$$

Note that if k=m, then $2\hat{n}(\mathbf{r}_k)\times\left(\nabla G(k,|\mathbf{r}_k-\mathbf{r}'_m|)\times\mathbf{J}_S^{(n)}(\mathbf{r}'_m)\right)=0$ (by continuity).

The simple form of (18) makes this iterative scheme easy to implement. Since ∇g can be calculated explicitly, it is easy to implement (18) in such a way that all quantities are calculated as needed. This means that the memory requirements are very modest, as no large matrices need to be stored. However, as the problem size increases, the time to produce e.g., $2\hat{n}(\mathbf{r}_k)\times\left(\nabla G(k,|\mathbf{r}_k-\mathbf{r}'|)\times\mathbf{J}_S^{(n)}(\mathbf{r}'_m)\right)$ repeatedly (and for all combinations of $\mathbf{r}_k,\mathbf{r}'_m,\ k\neq m$) increases. With a larger amount of memory (RAM) available, the iteration (18) can be formulated as a matrix – vector multiplication, where the matrix (matrices) is calculated only once, and then stored in memory for repeated use. To see the structure of this matrix multiplication, we need scalar components of the currents $\mathbf{J}_S^{(n)}(\mathbf{r})$. This can be achieved by introducing, at each triangle T_k, two orthogonal vectors $\mathbf{e}_k$ and $\mathbf{f}_k$ tangential to T_k. The current $\mathbf{J}_S^{(n)}(\mathbf{r})$ can then be represented by two Nx1 column vectors $\alpha^{(n)}$, $\beta^{(n)}$, where $\mathbf{J}_S^{(n)}(\mathbf{r}_k)=\alpha^{(n)}(k)\mathbf{e}_k+\beta^{(n)}(k)\mathbf{f}_k,\ 1\le k\le N$.

With $\mathbf{J}_S^{n+1}(\mathbf{r}_k)=d\alpha^{n+1}(k)\mathbf{e}_k+d\beta^{n+1}(k)\mathbf{f}_k,\ 1\le k\le N$, the recursion (18) becomes

$$\begin{pmatrix}d\alpha^{n+1}\\ d\beta^{n+1}\end{pmatrix}=a\left[\begin{pmatrix}-\alpha^{(n)}\\ -\beta^{(n)}\end{pmatrix}+\begin{pmatrix}A_{ee} & A_{fe}\\ A_{ef} & A_{ff}\end{pmatrix}\begin{pmatrix}\alpha^{(n)}\\ \beta^{(n)}\end{pmatrix}+\begin{pmatrix}\alpha^{(0)}\\ \beta^{(0)}\end{pmatrix}\right],\ 0<a\le 1,$$
$$\begin{pmatrix}\alpha^{(n+1)}\\ \beta^{(n+1)}\end{pmatrix}=\begin{pmatrix}\alpha^{(n)}\\ \beta^{(n)}\end{pmatrix}+\begin{pmatrix}d\alpha^{n+1}\\ d\beta^{n+1}\end{pmatrix},\ n=1,2,3,... \qquad (19)$$

In total, $\begin{pmatrix}\alpha^{(n)}\\ \beta^{(n)}\end{pmatrix}$ is 2N x 1, and the matrix $A=\begin{pmatrix}A_{ee} & A_{fe}\\ A_{ef} & A_{ff}\end{pmatrix}$ has format 2N x 2N.

Note that matrix A is independent of e.g. incident angle, which means that the vector $\begin{pmatrix}\alpha^{(n)}\\ \beta^{(n)}\end{pmatrix}$ can be replaced with a 2N x M matrix $\begin{pmatrix}\alpha_1^{(n)}\cdots\alpha_M^{(n)}\\ \beta_1^{(n)}\cdots\beta_M^{(n)}\end{pmatrix}$, where each $\begin{pmatrix}\alpha_k^{(n)}\\ \beta_k^{(n)}\end{pmatrix}$ represent a certain incident direction, $1\le k\le M$. On the other hand, the matrix A is valid only for a fixed frequency.

It should also be noted that the term IPO, is related to the choice of the initial current $\mathbf{J}_S^{(0)}(\mathbf{r})$. Namely, the choice of initial current has been seen to affect the convergence [17]. The initial current is chosen to be $\mathbf{J}_S^0(\mathbf{r})=2\hat{n}(\mathbf{r})\times\mathbf{H}_i(\mathbf{r})$ for all triangular facets that have an $\hat{n}$-component directed towards the transmitter. All other facets will have an initial current that is equal to 0. In addition, in the iteration process and when generating the A-matrix, the following shadowing condition is also considered. Namely, it is assumed that a current at a triangle with midpoint **r'** induces a current on a triangle with midpoint **r** only if

$\hat{n}(\mathbf{r})\cdot(\mathbf{r}-\mathbf{r}')<0$. Effectively, this means that a large portion of the entries in the matrix A will be zero. This condition is easy to implement and has shown to give relatively fast convergence even if it is not a reciprocal condition, see e.g. [18-19].

3.2.2 Mesh settings for the reference surface

The mesh of the reference surface consists of ~ 38 000 triangle facets and is shown in Figure 14. The smooth side and rough top surface consists of ~ 37 500 triangles within an area of $\pi r^2 = \pi \cdot 0.45^2 \sim 0.64$ m^2. Thus, the average side length of the triangles which representing the top and side surface of the rough background object is ~ 6 mm (~ $\lambda/5$). The smooth bottom surface (which is never illuminated) consists of ~ 500 triangles.

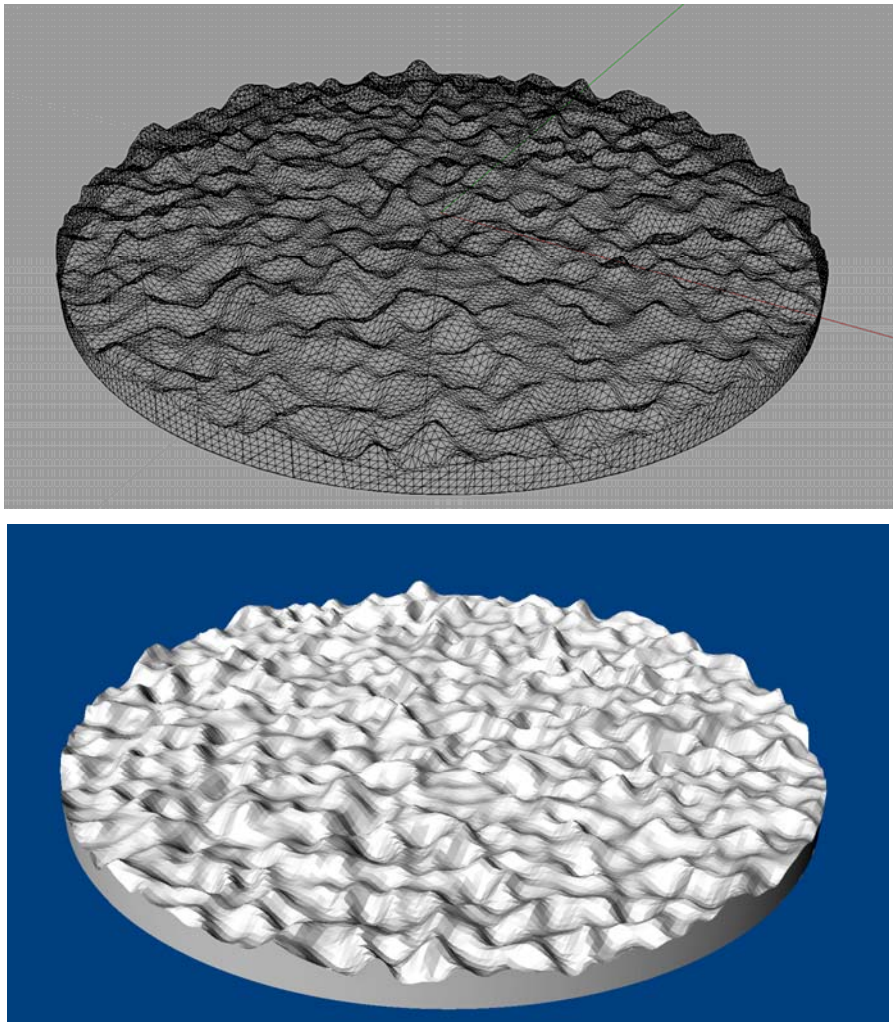

Figure 14. Top view: The mesh discretisation of the background surface. Bottom view: A rendered picture.

With this number of facets ~ 48 GB internal memory is required. The calculation time using 3 iterations, #ξ = 361, number of frequencies = 1 (i.e. 10 GHz) and one transmitter angle is ~ 100 minutes on an 8 core 2.4 MHz Pentium computer.

4 Results

The final results are normalized cross sections, σ_0 (dBm^2/m^2), for a fix transmitter antenna angle (α_T) and as a function of receiver antenna angle (α_R). The angle and polarisation definitions of the receiving and transmitting antennas are given in Figures 1-3. All data shown in this report are at the frequency 10 GHz.

The IPO results have been obtained by calculating the normalized cross section for turntable angles ξ = 0° - 360° in 10° steps, see Figure 15. To avoid contributions from the cylinder side of the rough surface only facets that are within the radius 0.4 meter is considered. The facet currents are then transformed into the electric far field vector. Thus, for each α_T and α_R we have obtained 36 vectors of the electric far field. The α_R range 0° to 180° is covered in 0.5° steps. The transformation from the electric far field vectors to normalised cross section can be made by averaging the vectors in different ways. Thus we define the following different normalised cross sections,

1. Total average $\quad \sigma_0 \propto \left\langle \left|\overline{E}\right|^2 \right\rangle / A$
2. Coherent average $\quad \sigma_0 \propto \left|\left\langle \overline{E} \right\rangle\right|^2 / A$
3. Incoherent average (diffuse) $\quad \sigma_0 \propto \left[\left\langle \left|\overline{E}\right|^2 \right\rangle - \left|\left\langle \overline{E} \right\rangle\right|^2 \right] / A$

where the area = A = $\pi r^2 = \pi \cdot 0.4^2$ m^2. Figure 15 shows IPO results where the total, coherent and incoherent averages are plotted.

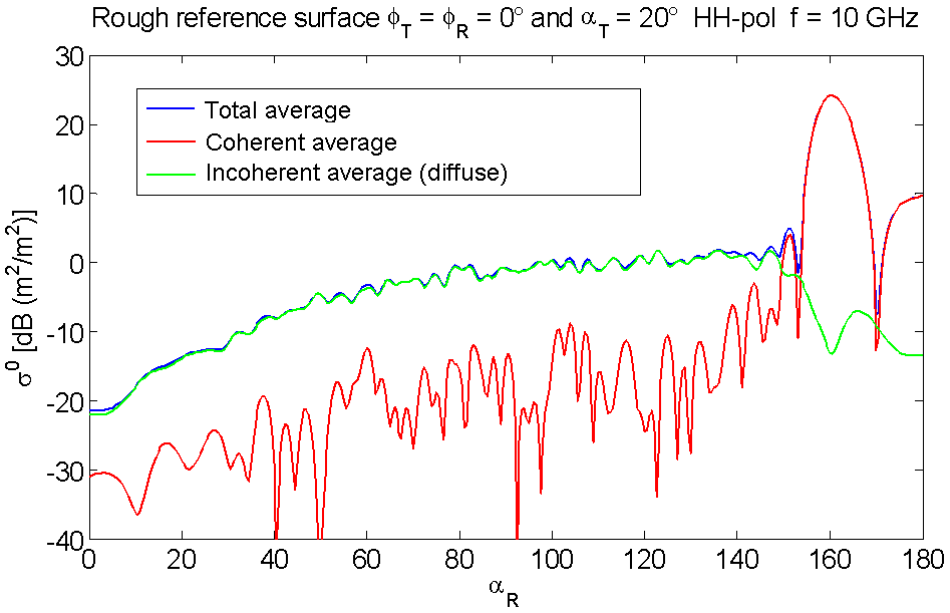

Figure 15. Normalized cross section results from IPO calculations for the rough reference PEC surface. The transmitting antenna depression angle α_T = 20° and the frequency is 10 GHz. The blue and red lines correspond to the incoherent and coherent average of 36 curves, each one corresponding to a ξ angle.

As can be seen in the Figure 15 the coherent part is only dominant in the $\alpha_R \sim 150° - 180°$ region. However, the diffuse scattering part is dominant in the $\alpha_R \sim 0° - 150°$ region.

The coherent part of the measured results are either cut in the analysis (i.e. in the $\alpha_R \sim 0° - \alpha_T$ region) or not measured (i.e. in the $\alpha_R \sim 150° - 180°$ region).

Thus, all data that are compared in this report are considered as the diffuse scattering part of the cross section from the rough reference surface.

Figure 16 - 20 shows the comparisons between IEM, IPO and measured normalized cross sections

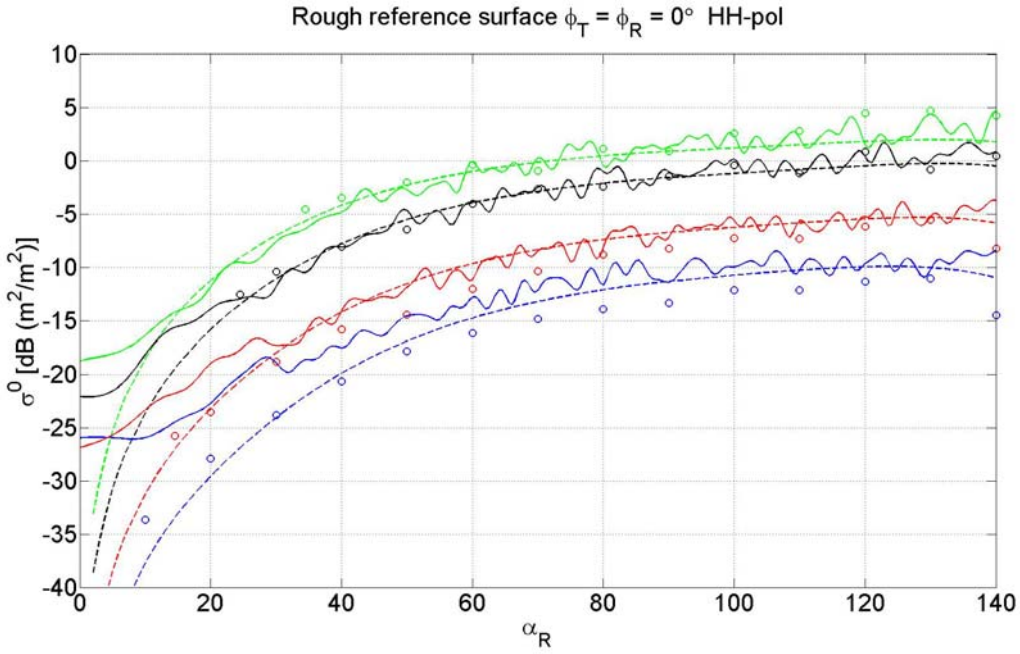

Figure 16. The bistatic normalised cross section for the reference surface at 10 GHz. The angles φ_T and φ_R (see definition in Figure 2) are 0°. The green, black, red and blue colour corresponds to elevation angles (α_T) of the transmitter antenna of 30°, 20°, 10° and 5°respectively. The solid lines represent results from IPO calculations, dashed lines are IEM results and dots are measurement results. The polarisation is HH according to the definition in Figure 6.

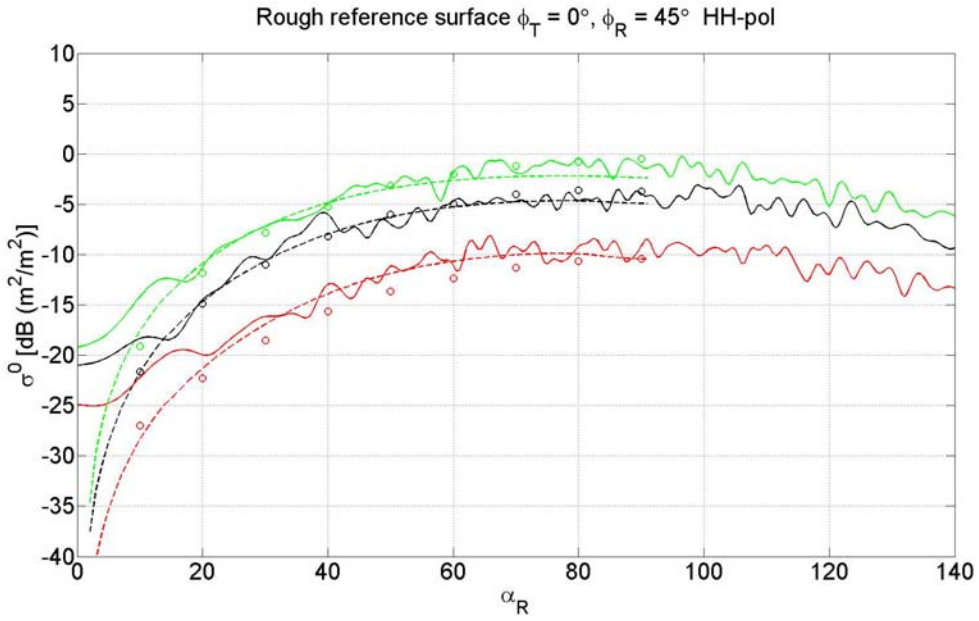

Figure 17. The bistatic normalised cross section for the reference surface at 10 GHz. The angle φ_R , which represents the angle between the quarter arc and the full arc, is 45°. The green, black and red colours correspond to elevation angles (α_T) of the transmitter antenna of 30°, 20° and 10° respectively. The solid lines represent results from IPO calculations, dashed lines are IEM results and dots are measurement results. The polarisation is HH according to the definition in Figure 6.

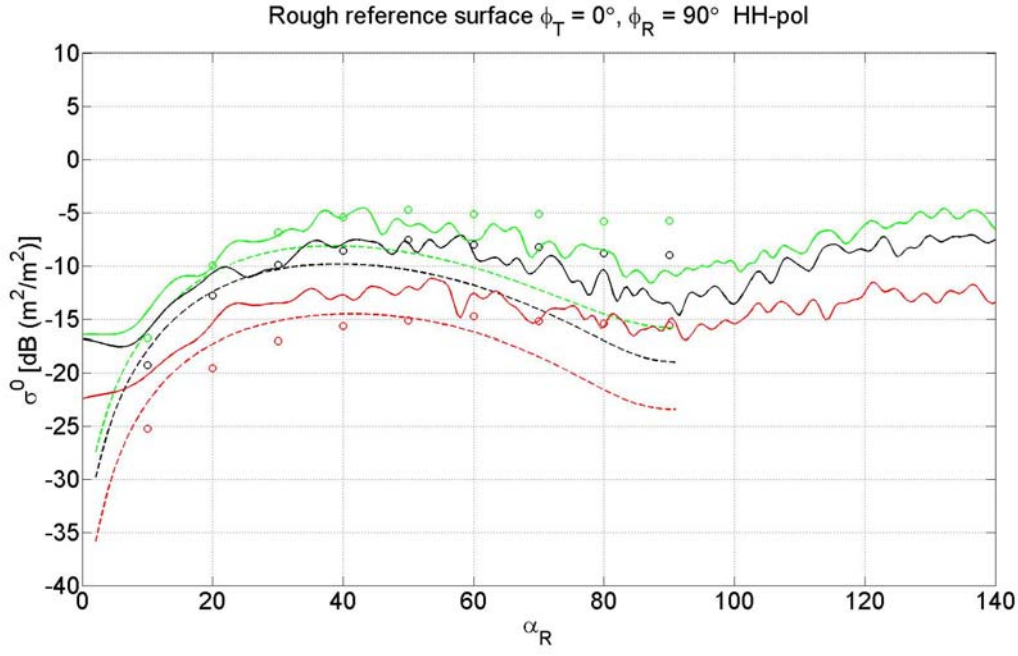

Figure 18. The bistatic normalised cross section for the reference surface at 10 GHz. The angle φ_R , which represents the angle between the quarter arc and the full arc, is 90°. The green, black and red colours correspond to elevation angles (α_T) of the transmitter antenna of 30°, 20° and 10° respectively. The solid lines represent results from IPO calculations, dashed lines are IEM results and dots are measurement results. The polarisation is HH according to the definition in Figure 6.

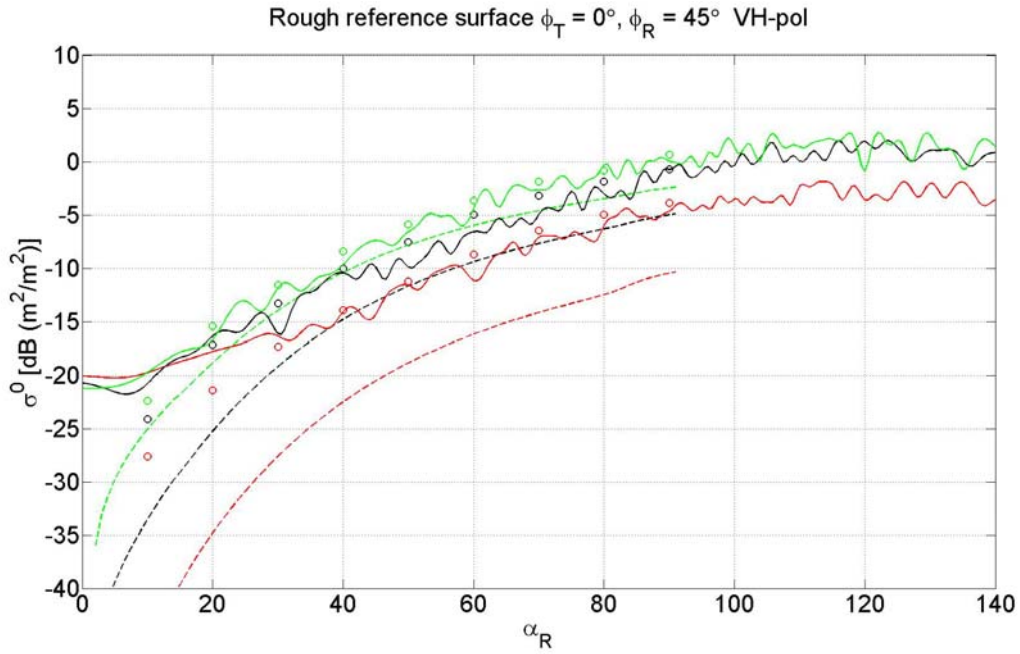

Figure 19. The bistatic normalised cross section for the reference surface at 10 GHz. The angle φ_R , which represents the angle between the quarter arc and the full arc, is 45°. The green, black and red colours correspond to elevation angles (α_T) of the transmitter antenna of 30°, 20° and 10° respectively. The solid lines represent results from IPO calculations, dashed lines are IEM results and dots are measurement results. The polarisation is VH according to the definition in Figure 6.

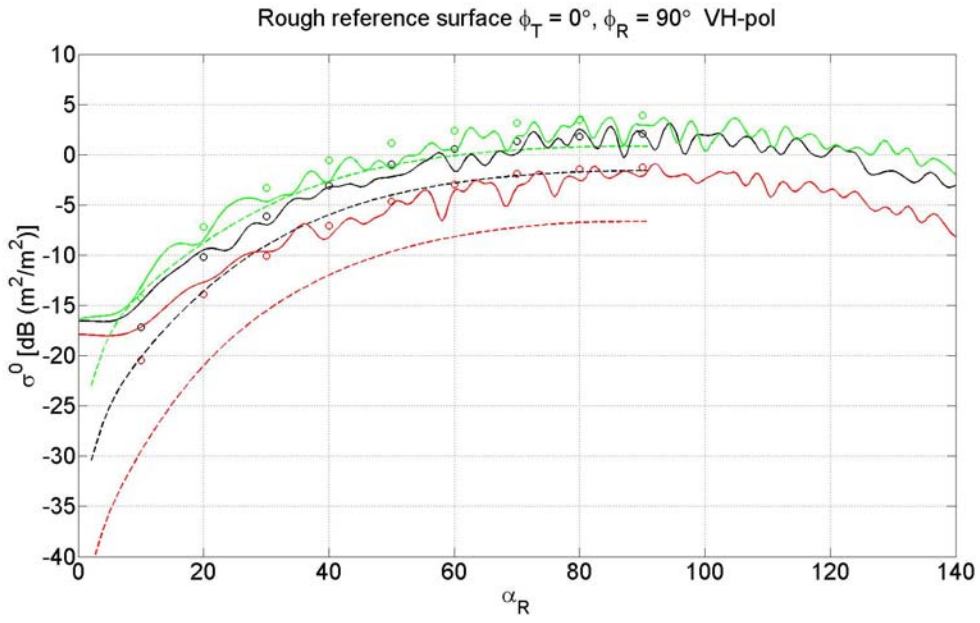

Figure 20. The bistatic normalised cross section for the reference surface at 10 GHz. The angle φ_R , which represents the angle between the quarter arc and the full arc, is 90°. The green, black and red colours correspond to elevation angles (α_T) of the transmitter antenna of 30°, 20° and 10° respectively. The solid lines represent results from IPO calculations, dashed lines are IEM results and dots are measurement results. The polarisation is VH according to the definition in Figure 6.

5 Analysis

Before analysing the results it is worth stressing that there are some different assumptions made in the calculations. For example, the IPO calculations include 3 iterations (which correspond to 3 internal reflections in a ray tracing approach) and in addition a shadowing function is applied for each iteration step. The IEM calculations are made without any internal reflection interactions but with a shadowing function included. The IPO calculations have been made in the far field region while near field corrections have been applied to the IEM calculations. However, these near field corrections have been shown to be relatively small.

The calculation (CPU) time for IPO is heavily dependent on number of facets that are describing the object. IEM, on the other hand, is based on calculating an average value of the diffuse part of the normalized cross section by describing the roughness of a surface by two statistical measures, i.e. the correlation length and the height standard deviation. This makes the IEM on the order of magnitude faster, in terms of CPU-time, than IPO. Thus, IEM is a suitable method when calculating the normalized cross section from a rough surface while IPO is a suitable method in other applications, e.g. calculating the RCS for a manmade object.

The general trend is that the agreement between the calculations (both IEM and IPO) and measurement results are getting better for larger α_T. Although the calculating methods are relatively different in character (one deterministic and one statistical based) the results shows encouraging similarities, both in shape and absolute level.

The IPO results exhibit relatively good agreement with the measurement results for all polarisation and bistatic geometry combinations. It is only in the $\alpha_R = 0° - \sim 20°$ region where one can see a deviating trend between the IPO and measured results. The reason for this is to be investigated. However, Figure 18 exhibit a relative large deviation in absolute value (up to 5 dB) between IPO and measured results.

The IEM results exhibit very good agreement to the measurement results for HH-polarisation and $\varphi_R = \varphi_T = 0°$ and $\varphi_T = 0°$ $\varphi_R = 45°$, see Figures 16 and 17. For the other polarisation and geometry combinations it seems that the IEM results underestimates the cross sections, see Figures 18 - 20. The deviations are more pronounced for lower transmitter elevation angles (α_T). The reason for this needs to be investigated. However, the shapes of the IEM results are in well agreement with the measured results.

6 Summary and conclusions

Bistatic radar measurements have been performed on a manufactured rough aluminum surface. The measurements were conducted at the FOIs outdoor facility “Lilla Gåra”. The extracted normalized cross sections from the measurements are used to validate two different calculation methods, i.e. the iterative physical optics (IPO) method and the integral equation method (IEM). The IPO method is based on solving the magnetic field integral equation (MFIE) iteratively by including shadowing conditions in the iterations. The method requires a faceted representation of the object and each iteration step can be considered as an internal interaction contribution to the cross section. The IEM method is based on solving the Stratton-Chu integral equation by describing the roughness of the surface using two statistical measures, the correlation length, L, and the height deviation, σ_H. The roughness is given by two statistical parameters while the output is given as the expectation value of the diffuse part of the normalized cross section. There are several variants of IEM in the literature, e.g. with and without shadowing functions and with and without multiple reflections. We are using an IEM variant that includes shadowing but not multiple reflections.

The comparison between the calculated and measured results exhibit good agreements. The results from the measurement and IPO are generally in good agreement over all geometries and polarization combinations, see Figures 16 - 20. The IEM results exhibit very good agreement with IPO and measurement results when the polarization is HH and $\varphi_R = \varphi_T = 0°$ or $\varphi_T = 0°$ $\varphi_R = 45°$, see Figures 16 and 17. For the other geometry and polarisation combinations the IEM results will tend to underestimate the normalised cross sections.

Due to the fact that IEM is a very fast method, in terms of CPU-time and relative to other methods, the results are encouraging. The goal is to use IEM as a complementary method when modeling the background and/or target-background interaction contribution to the cross section for large scenarios, e.g. a ship on sea.

The conclusion is that the IEM method has potential to be used to model backgrounds and target-background interaction contributions. Further investigations have to be made concerning variance measures of the diffuse part of the normalized cross section, the impact of material properties and how to combine e.g. PO calculations with IEM calculations to be able to make calculations on large scenarios.

7 References

[1] Technical Arrangement No. 4.4 'New models for radar targets and environment' FOI Diarie nr. 08-H184:2

[2] Work Breakdown Structure (WBS) of Technical Arrangement No 4.4. Draft date 080615

[3] E. Zdansky, J. Rahm and A. Örbom, "Bistatic RCS measurement on different background surfaces", FOI-R--2785--SE Linköping 2009.

[4] S. Nilsson, M. Wilow, N. Karlsson och A. Örbom, "Improvements of the Swedish outdoor RCS measurement capability", *AMTA Europe Symposium*, München, 1-4 maj 2006, Conference proceedings 118-123.

[5] J.Rasmusson, N. Gustafsson och J. Rahm, "Outdoor broadband RCS measurements of model-scale aircraft", *AMTA*, Cleveland USA, 3-8 november 2002 Conference proceedings 439-444 (FOI-S--0698-SE).

[6] T.-K. Chan, Y. Kuga, A. Ishimaru and C.T.C. Le, "Experimental studies of bistatic scattering from two-dimensional conducting random rough surfaces", *IEEE Trans. on Geoscience and Remote Sensing* **34**(3) (1996).

[7] E. Zdansky, "Kalibrering av radarmålarea, särskilt objektfri kalibrering", FOI-R--2442--SE Linköping 2007.

[8] E. Zdansky, A. Örbom, "Kalibrering av logaritmisk magnituddetektor", FOI-R--2441--SE Linköping 2007.

[9] E. Zdansky, A. Örbom, "Prov med objektfri kalibrering av radarmålarea", FOI-R--2443--SE Linköping 2007.

[10] A. K. Fung, "Microwave Scattering and Emission Models and Their Application". Boston: Artech House, 1994.

[11] A. K. Fung, Z. Li and K. S. Chen, The Improved IEM Surface Scattering Model (IIEM), *J. Electromagn. Wave Appl,* vol. 16, pp. 689-702, 2002.

[12] C. K.-S. Wu Tzong-Dar, "A Reappraisal of the Validity of the IEM Model for Backscattering From Rough Surfaces " *IEEE Trans. on Geoscience and Remote Sensing,* vol. 42, pp. 743-752, 2004.

[13] M. Gustafsson, S. Nilsson, J. Rahm and E. Zdansky, "Modelleringsmetoder för bistatisk markspridning – Litteraturstudie -" FOI-R--0825--SE

[14] B. G. Smith, "Geometrical Shadowing of a Random Rough Surface" *IEEE Trans. on Antennas and Propagation*, vol. 15, pp. 668-671, 1967.

[15] M. I. Sancer, "Shadow-Corrected Electromagnetic Scattering from randomly Rough Surface" *IEEE Trans. on Antennas and Propagation*, vol 17, pp. 577-585, 1969

[16] Fernando Obelleiro-Basteiro, Jose Luis Rodriguez and Robert J. Burkholder, "An Iterative Physical Optics Approach for Analyzing the Electromagnetic Scattering by Large Open-Ended Cavities", *IEEE Trans. Antennas and Propagation,* Vol. 43, No. 4, pp. 356-361, April 1995.

[17] Robert J. Burkholder, "A Fast and Rapidly Convergent Iterative Physical Optics Algorithm for Computing the RCS of Open-Ended Cavities", *ACES Journal*, Vol. 16, No. 1, March 2001.

[18] Robert J. Burkholder and Tomas Lundin, “Forward-Backward Iterative Physical Optics Algorithm for Computing the RCS of Open-Ended Cavities”, *IEEE Trans. Antennas and Propagation,* Vol. 53, No. 2, pp. 793-799, February 2005.

[19] Jonas Rahm och Magnus Gustafsson, “ Iterativ fysikalisk optik (IPO) – En studie”, FOI-R--2416--SE, December 2007.

Appendix A: Measured reflectivity

The table presents the measured normalised cross section results for the different antenna angle combinations on the metallic rough surface. The antenna angles, α and φ of the transmitter, T, and receiver, R, are defined in Figures 1 and 2.

Angle combination	α_T	φ_T	α_R	φ_R	σ^0_{HH} [dB] (10 GHz)	σ^0_{VH} [dB] (10 GHz)
1	10˚	0˚	10˚	90˚	-25.3	-20.5
2	10˚	0˚	20˚	90˚	-19.6	-13.9
3	10˚	0˚	30˚	90˚	-17.0	-10.1
4	10˚	0˚	40˚	90˚	-15.7	-7.1
5	10˚	0˚	50˚	90˚	-15.2	-4.6
6	10˚	0˚	60˚	90˚	-14.7	-2.9
7	10˚	0˚	70˚	90˚	-15.2	-1.9
8	10˚	0˚	80˚	90˚	-15.5	-1.5
9	10˚	0˚	90˚	90˚	-15.6	-1.3
10	20˚	0˚	10˚	90˚	-19.3	-17.2
11	20˚	0˚	20˚	90˚	-12.8	-10.2
12	20˚	0˚	30˚	90˚	-9.9	-6.1
13	20˚	0˚	40˚	90˚	-8.6	-3.1
14	20˚	0˚	50˚	90˚	-7.6	-1.0
15	20˚	0˚	60˚	90˚	-8.0	0.5
16	20˚	0˚	70˚	90˚	-8.2	1.4
17	20˚	0˚	80˚	90˚	-8.8	1.8
18	20˚	0˚	90˚	90˚	-9.0	2.1
19	30˚	0˚	10˚	90˚	-16.7	-14.3
20	30˚	0˚	20˚	90˚	-10.0	-7.2
21	30˚	0˚	30˚	90˚	-6.8	-3.3
22	30˚	0˚	40˚	90˚	-5.4	-0.6
23	30˚	0˚	50˚	90˚	-4.7	1.2
24	30˚	0˚	60˚	90˚	-5.2	2.4
25	30˚	0˚	70˚	90˚	-5.2	3.1
26	30˚	0˚	80˚	90˚	-5.8	3.4
27	30˚	0˚	90˚	90˚	-5.8	3.9
28	10˚	0˚	10˚	45˚	-27.0	-27.6
29	10˚	0˚	20˚	45˚	-22.3	-21.4
30	10˚	0˚	30˚	45˚	-18.5	-17.3
31	10˚	0˚	40˚	45˚	-15.7	-13.9
32	10˚	0˚	50˚	45˚	-13.7	-11.3
33	10˚	0˚	60˚	45˚	-12.4	-8.7
34	10˚	0˚	70˚	45˚	-11.3	-6.5
35	10˚	0˚	80˚	45˚	-10.7	-5.0
36	10˚	0˚	90˚	45˚	-10.4	-3.9
37	20˚	0˚	10˚	45˚	-21.6	-24.1
38	20˚	0˚	20˚	45˚	-14.9	-17.1
39	20˚	0˚	30˚	45˚	-11.0	-13.3

Angle combination	α_T	φ_T	α_R	φ_R	σ^0_{HH} [dB] (10 GHz)	σ^0_{VH} [dB] (10 GHz)
40	20˚	0˚	40˚	45˚	-8.2	-10.0
41	20˚	0˚	50˚	45˚	-6.0	-7.5
42	20˚	0˚	60˚	45˚	-4.9	-5.0
43	20˚	0˚	70˚	45˚	-4.0	-3.2
44	20˚	0˚	80˚	45˚	-3.6	-1.9
45	20˚	0˚	90˚	45˚	-3.7	-0.7
46	30˚	0˚	10˚	45˚	-19.1	-22.4
47	30˚	0˚	20˚	45˚	-11.8	-15.5
48	30˚	0˚	30˚	45˚	-7.8	-11.6
49	30˚	0˚	40˚	45˚	-5.2	-8.4
50	30˚	0˚	50˚	45˚	-3.2	-5.9
51	30˚	0˚	60˚	45˚	-2.0	-3.6
52	30˚	0˚	70˚	45˚	-1.2	-1.9
53	30˚	0˚	80˚	45˚	-0.8	-0.8
54	30˚	0˚	90˚	45˚	-0.5	0.6
55	5˚	0˚	10˚	0˚	-33.6	-
56	5˚	0˚	20˚	0˚	-27.9	-
57	5˚	0˚	30˚	0˚	-23.8	-
58	5˚	0˚	40˚	0˚	-20.6	-
59	5˚	0˚	50˚	0˚	-17.9	-
60	5˚	0˚	60˚	0˚	-16.2	-
61	5˚	0˚	70˚	0˚	-14.9	-
62	5˚	0˚	80˚	0˚	-14.0	-
63	5˚	0˚	90˚	0˚	-13.3	-
64	5˚	0˚	100˚	0˚	-12.1	-
65	5˚	0˚	110˚	0˚	-12.1	-
66	5˚	0˚	120˚	0˚	-11.3	-
67	5˚	0˚	130˚	0˚	-11.1	-
68	5˚	0˚	140˚	0˚	-14.5	-
69	30˚	0˚	34.5˚	0˚	-4.6	-
70	30˚	0˚	40˚	0˚	-3.5	-
71	30˚	0˚	50˚	0˚	-2.0	-
72	30˚	0˚	60˚	0˚	-0.4	-
73	30˚	0˚	70˚	0˚	-1.0	-
74	30˚	0˚	80˚	0˚	1.1	-
75	30˚	0˚	90˚	0˚	0.9	-
76	30˚	0˚	100˚	0˚	2.6	-
77	30˚	0˚	110˚	0˚	2.8	-
78	30˚	0˚	120˚	0˚	4.4	-
79	30˚	0˚	130˚	0˚	4.7	-
80	30˚	0˚	140˚	0˚	4.2	-